Effect of Vapor-Cell Geometry on Rydberg-Atom-Based Measurements of Radio-Frequency Electric Fields

Haoquan Fan, Santosh Kumar, Jiteng Sheng, James P. Shaffer, Christopher L. Holloway, and Joshua A. Gordon

Phys. Rev. Applied **4**, 044015 — Published 22 October 2015

DOI: 10.1103/PhysRevApplied.4.044015

Effect of Vapor Cell Geometry on Rydberg Atom-based Radio-frequency Electric Field Measurements

Haoquan Fan, Santosh Kumar, Jiteng Sheng, and James P. Shaffer*
Homer L. Dodge Department of Physics and Astronomy, The University of Oklahoma, 440 W. Brooks St. Norman, OK 73019

Christopher L. Holloway and Joshua A. Gordon
National Institute of Standards and Technology, Electromagnetics Division, 325 Broadway, Boulder, CO 80305
(Dated: September 25, 2015)

A new approach to detect absolute radio-frequency (RF) electric fields (E-fields) that uses Rydberg atoms at room temperature in vapor cells has recently been demonstrated. The large transition dipole moments between energetically adjacent Rydberg states enable this technique to make traceable E-field measurements with high sensitivity over a large frequency range, from 1 GHz to 1 THz. In this paper, we experimentally investigate how the vapor cell geometry affects the accuracy of the measurements. We find that the effects of the vapor cell on the measured RF E-field can be minimized by making the vapor cell size small compared to the wavelength of the RF E-field.

I. INTRODUCTION

Precision measurements using atoms and molecules are exceptionally useful as standards of time and length. Measurement of magnetic and electric fields [1–4], can also be improved with atom-based methods. Atom-based standards have the advantages of being linked to precision measurements of fundamental constants and atomic, or molecular, properties [5].

Radio-frequency (RF) fields are the basis of modern communications [6], remote sensing [7] and many other applications [8]. In contrast to progress on measuring time, frequency, and magnetic fields; RF electric field (E-field) measurement has changed little since the dipole antenna was developed [9]. The sensitivity of current RF E-field standards is $\sim 1\mathrm{mVcm}^{-1}\mathrm{Hz}^{-1/2}$ with an accuracy of $5\% \sim 20\%$ depending on the frequency range. Recently, work on atom-based E-field measurements has surpassed these limits [10–15] due to advances in coherent sub-Doppler spectroscopy of Rydberg atoms using electromagnetically induced transparency (EIT) [16–18]. The method uses EIT [19] to perform the RF E-field measurement using alkali atoms placed in a vapor cell at room temperature. The atoms are partially excited to Rydberg states to determine the amplitude of a RF E-field. Compared to previous atomic microwave power standards [20–23], this method measures the RF E-field using Rydberg states rather than ground state atoms. Using this approach, RF E-fields can be measured with high sensitivity, $\sim 30\mu\mathrm{Vcm}^{-1}\mathrm{Hz}^{-1/2}$ [10], over a large frequency range, 1 GHz $\sim$ 1 THz, due to the large transition dipole moments between Rydberg states, reaching values several thousand times larger than the D_2 transitions of alkali atoms [24]. Of course, the sensitivity is not the same over this entire frequency range. Some of the most salient effects influencing the sensitivity in different frequency regimes are described in [25]. Recently, RF E-field spatial distributions were mapped using this approach with high resolution, $\sim \lambda_{\mathrm{RF}}/650$ [12, 15], where λ_{RF} is the wavelength of the RF E-field. It has also been shown that the method can be used to sense the vector RF E-field [11]. As a result, Rydberg atom-based RF E-field sensing is a promising candidate for a new standard for RF E-fields. RF E-fields can also be used to manipulate Rydberg atoms in micron-sized vapor cells [26, 27]. RF E-fields and how they can be used to coherently control atoms can also be important for quantum information science and other sensing applications, significantly broadening the scientific interest in the interaction between RF E-fields and vapor cells.

To apply Rydberg atom-based RF E-field detection in practice, the accuracy of the method needs to be studied. The vapor cell is one of the factors that determines the accuracy. The atoms are confined in a vapor cell which is typically made of pyrex or quartz. RF E-fields can be absorbed or reflected by the walls of the vapor cells. Although the reflection and absorption can be made to be small by choosing suitable materials, variation of the RF E-field can arise from the Fabry-Perot (FP) effect, absorption by the vapor cell surface as the RF E-field passes through to interact with the atoms, and polarization of the vapor cell resulting from the E-field interacting with the dielectric material. The FP effect occurs because when a RF wave is incident onto a hollow glass vapor cell, standing waves can develop inside the vapor cell due to reflections from the glass walls, forming a RF FP cavity. The distribution of the E-field inside the vapor cell will vary depending on the frequency of the RF E-field and on the size of the vapor cell. The FP effect can result in the measured E-field being different from the incident field, the desired quantity. The corners and imperfections of a vapor cell can also re-scatter and re-radiate the RF E-field and cause the measured RF E-field to be different from the incident E-field signal.

In this paper, we show the accuracy of RF E-field measurement depends on the geometry of the vapor cell. The accuracy is dependent on the ratio of vapor cell size, D, of the cubic pyrex vapor cells used for the measurements

* Corresponding author: shaffer@nhn.ou.edu

to the RF E-field wavelength, $\lambda_{\rm RF}$, i.e. D/$\lambda_{\rm RF}$. By making the ratio of vapor cell size to wavelength small, we show experimentally that the accuracy is greater than current methods in the frequency range, 10-30 GHz, and is not limited by the vapor cell geometry provided D/$\lambda_{\rm RF} < 0.1$.

II. EXPERIMENT

Our method utilizes EIT to measure the RF E-field. Changes in the probe laser absorption as a function of the probe laser frequency are measured. A counter-propagating coupling laser excites the atoms to a Rydberg state to generate a transmission window for the probe laser. The transmission window is the result of EIT [19]. A RF E-field resonant with a transition from the upper state of the EIT system to another Rydberg state can cause the EIT window to split into two peaks with proper selection of laser polarization. This is called Autler-Townes (AT) splitting [28]. The AT splitting is proportional to the amplitude of the RF E-field [10]. The AT frequency splitting, Δ, is

$$\Delta = \frac{\lambda_{\rm c}}{\lambda_{\rm p}} \frac{\mu_{\rm RF} {\rm E}}{\rm h}, \qquad (1)$$

where $\lambda_{\rm p}$ and $\lambda_{\rm c}$ are the wavelengths of the probe and coupling lasers, respectively. $\mu_{\rm RF}$ is the transition dipole moment, E is the amplitude of the RF E-field, and h is Planck's constant. We assume the probe laser is scanned to observe the AT splitting here. The wavelength mismatch of the counter-propagating lasers with the Doppler effect accounts for the factor of $\lambda_{\rm c}/\lambda_{\rm p}$ in Eq. (1) [10, 16].

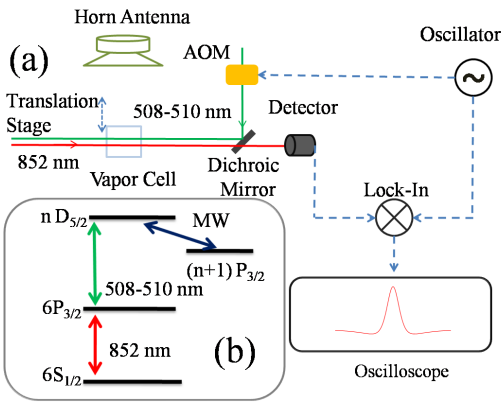

FIG. 1. (color online) Setup and energy level diagram for the experiments. (a) The experimental setup. The probe and coupling lasers are overlapped inside the vapor cell and the RF horn antenna is placed in the far field limit. (b) The energy level diagram. The 852 nm and $508-510$ nm lasers are the EIT probe and coupling lasers, respectively. The RF E-field couples to the $nD_{5/2} \leftrightarrow (n+1)P_{3/2}$ transitions.

Fig. 1(a) shows the experimental setup and Fig. 1(b) shows the energy level diagram for Cesium (Cs) as used in the experiments. The frequency of the probe laser, ~ 852 nm, is set to the Cs $6S_{1/2}(F=4)$ to $6P_{3/2}(F=5)$ transition. The frequency of the coupling laser, $\sim 508-510$ nm, is set to excite the upper transition of the cascade system, corresponding to the Cs $6P_{3/2}(F=5) \leftrightarrow nD_{5/2}$ transition shown in Fig. 1(b). Both lasers are locked to a high-finesse FP cavity and shaped as Gaussian beams using optical fibers. The beam radii are 156 μm for the probe laser and 210 μm for the coupling laser. The lasers counter-propagate in an overlapping geometry inside the vapor cell with beam waist at the center of the vapor cell. The linewidths of both lasers are ≤ 100 kHz. An RF signal generator drives the horn antenna to generate RF E-field. The horn antenna is placed in the far field and coupled to the $nD_{5/2} \leftrightarrow (n+1)P_{3/2}$ transition. The transitions between Rydberg states involved in our experiment correspond to n = 32, 34, 35, 39, 44, 48, 61, and 69, which have RF frequencies of 23.91 GHz, 19.64 GHz, 17.84 GHz, 12.06 GHz, 8.57 GHz, 6.49 GHz, 3.06 GHz, and 2.08 GHz, respectively.

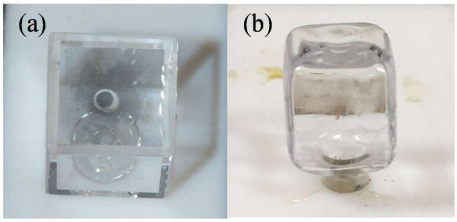

FIG. 2. (color online) The vapor cells used in the experiment. (a) The vapor cell with 8 mm inner diameter and 1 mm wall thickness. (b) The vapor cell with 9 mm inner diameter and 1.25 mm wall thickness.

The vapor cells used in the experiments are cubic and made of pyrex as shown in Fig. 2. Fig. 2(a) shows an 8 mm vapor cell, with a wall thickness of 1 mm, giving size to wavelength ratios, D/$\lambda_{\rm RF}$, of 0.64, 0.52, 0.48, 0.34, 0.23, 0.17, 0.08, and 0.05. The size of the other vapor cell, as shown in Fig. 2(b), is 9 mm with 1.25 mm wall thickness, yielding size to wavelength ratios of 0.72, 0.59, 0.53, 0.36, 0.26, 0.19, 0.09, and 0.06. We chose this range of D/$\lambda_{\rm RF}$ ratios because the wavelengths vary from, 1.25 cm, around the size of the vapor cells to 14.42 cm, around an order of magnitude more than the size of the vapor cell. The vapor cell size is defined to be the inner diameter of the vapor cell. The vapor cells are placed on a translation stage and mounted on a teflon block. This allows the cross-section of vapor cell to be scanned across the lasers in order to map the field variability and distribution inside the vapor cell, similar to the experimental setups used in [12, 15]. The position of the vapor cells relative to the laser beams can be scanned at a precision of 0.01 mm. To avoid the effect of RF E-field reflections from the apparatus, we placed RF absorbers around the interaction area.

To obtain high signal-to-noise ratio, the coupling laser is amplitude-modulated with an acoustic-optical mod-

ulator at 50 kHz. The transmitted probe signal is recorded by a photodiode and demodulated using a lock-in-amplifier. The demodulated signal from the lock-in amplifier is recorded on a digital oscilloscope.

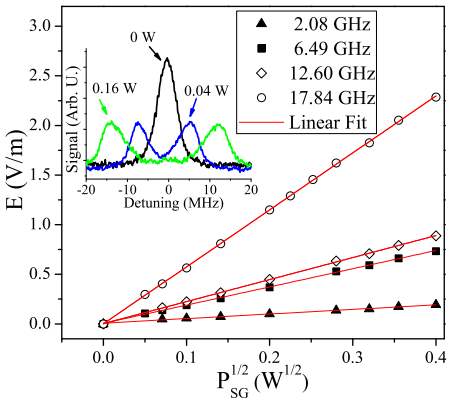

FIG. 3. (color online) Experimental data for RF E-field amplitude with a cubic vapor cell with 8 mm inner diameter as a function of the square-root of power at the RF signal generator. The inset shows raw data for 2.08 GHz.

To demonstrate that the AT splitting, Δ, is linearly dependent on RF E-field amplitude, E, we took data varying the power of the RF signal generator at the different RF E-field frequencies used for the vapor cell geometry experiments. Fig. 3 shows the square root of the RF power, P_{SG}, versus the measured RF E-field amplitudes which are derived from Eq. (1). P_{SG} of the RF E-field is directly taken from the RF signal generator and the amplitudes of the RF E-fields are determined by the AT splitting. We calculated transition dipole moments used for the analysis to be: $\mu_{RF} = 3221.5\ e\ a_o$ for the $69D_{5/2} \leftrightarrow 70P_{3/2}$ transition at 2.08 GHz where a_o is Bohr radius, and e is the electric charge, $\mu_{RF} = 1508.9\ e\ a_o$ for the $48D_{5/2} \leftrightarrow 49P_{3/2}$ transition at 6.49 GHz , $\mu_{RF} = 971.2\ e\ a_o$ for the $39D_{5/2} \leftrightarrow 40P_{3/2}$ transition at 12.60 GHz, and $\mu_{RF} = 770.0\ e\ a_o$ for the $35D_{5/2} \leftrightarrow 36P_{3/2}$ transition at 17.84 GHz. The transition dipole moments include both the angular and radial parts. The angular part is 0.49 for a $nD_{5/2} \leftrightarrow (n+1)P_{3/2}$ transition, while the radial part can be calculated by numerically solving Schrödinger equation using a model potential fit to several experimentally determined energy levels [29]. The linear fit shows the RF E-field amplitudes are proportional to the square root of P_{SG}. This validates our method for measuring the RF E-field in the vapor cell.

III. RESULTS

The interaction between the RF E-field and a dielectric material can be described by the complex permittivity of the dielectric material [30],

$$\varepsilon = \varepsilon' + \mathrm{i}\varepsilon'', \tag{2}$$

where ε is the relative permittivity, and ε', ε'' are the real and imaginary parts of complex permittivity, respectively. The RF E-field dispersion can be described by the real part, ε', while the absorption is proportional to the imaginary part, ε''. The loss tangent,

$$\mathrm{Tan}(\delta) = \frac{\varepsilon''}{\varepsilon'}, \tag{3}$$

determines the absorption at a fixed wavelength. As a rule of thumb, for a good absorber, $\mathrm{Tan}(\delta) \geq 0.1$, while those with $\mathrm{Tan}(\delta) \leq 0.01$ can be considered transparent to RF E-fields. The real dielectric constant for pyrex, ε', is ~ 4.6 and the imaginary part, ε'', is ~ 0.023 in the GHz RF frequency range. These yield $\mathrm{Tan}(\delta) = 0.005$ for pyrex [31]. The RF E-field decay with propagation distance, d, in a dielectric material is determined by,

$$\mathrm{E} = \mathrm{E_0 Exp}\Big[-\frac{2\pi}{\lambda_{\mathrm{RF}}}\Big(\frac{\delta \mathrm{d}}{2}\Big)\Big], \tag{4}$$

where $\mathrm{E_0}$, and E are the incident and transmitted RF E-field amplitudes, respectively. For a RF E-field at 12.6 GHz, the absorption by 1 mm of pyrex is 0.066%. Thus, the absorption effects are small and can be ignored in this work.

Fig. 4. shows the variation of the RF E-field inside the vapor cells for different D/λ_{RF} ratios. We observe that the RF E-field variation decreases when the D/λ_{RF} ratio becomes smaller. This is consistent with the theory of a FP cavity as discussed in the introduction. When the wavelength of the RF E-field is comparable to, or smaller than, the size of the vapor cells, it produces interference. When D is smaller than $\sim \lambda_{\mathrm{RF}}/4$, the interference inside the vapor cell is greatly reduced because the vapor cell cannot support a resonance. The cross section for scattering also decreases as the vapor cell size becomes small compared to λ_{RF}. To quantify the effect, we fit the data using a quadratic equation. The Taylor expansion of the RF E-field should be constant if there is no effect from the vapor cell walls and we assumed the incident RF E-field is a plane wave. Higher order terms indicate variation of the RF E-field in the vapor cell. For example, the quadratic term shows the curvature of the RF E-field. The fits show that when the $\mathrm{D}/\lambda_{\mathrm{RF}}$ ratio is smaller than 0.1, the field variation is $\sim 1\%$. The 1% variation is mostly due to measurement uncertainty. For example, if we fit the data for $\mathrm{D}/\lambda_{\mathrm{RF}} = 0.09$ in Fig.4, the average value of the AT splitting is 20.51 MHz and the standard variation is ± 0.14 MHz. This gives a variation of $\leq \pm 0.7\%$. The average linear variation is $\sim 1\%$ of the constant term across the vapor cell while the average quadratic variation across the vapor cell is $\sim 0.3\%$ of the constant term. These results indicate that under these conditions the RF E-field is approximately constant. High order terms than

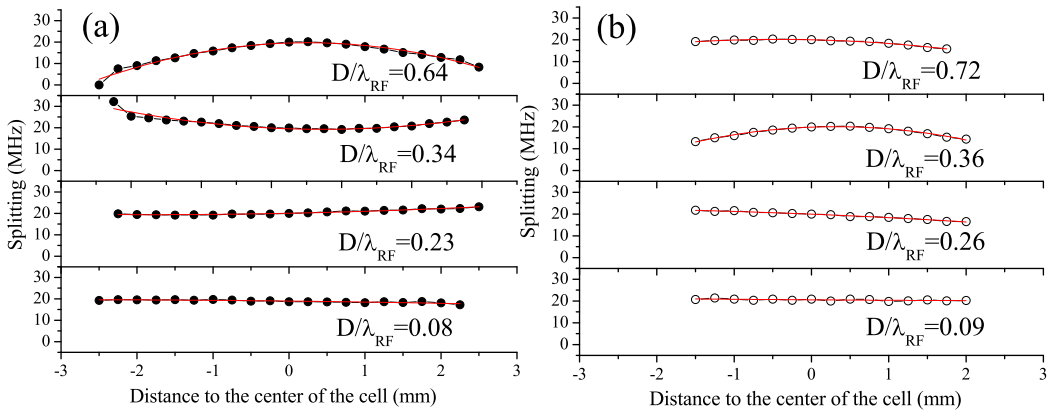

FIG. 4. (color online) Data generated by scanning the position of the EIT detection beams through the vapor cells at different D/λ_{RF} ratios where D is the size of the vapor cells and λ_{RF} is the wavelength of RF E-field. The experiment involves two vapor cells both of which show the same effect. (a) The black dots represent the 8 mm inner diameter vapor cell. (b) The hollow circles represent the 9 mm inner diameter vapor cell. The red lines are a quadratic fit. The variation becomes smaller as D/λ_{RF} decreases. The distance is measured from the vapor cell wall where the RF E-field is incident, while the vertical axis is the AT splitting caused by RF E-field. The data does not cover the same range of distances because the quality of the windows for the conventionally constructed vapor cell is not optically flat at the edges, see Fig. 2.

the quadratic one are smaller yet also indicating that under these conditions the RF E-fields are not significantly perturbed by the vapor cell compared to the statistical measurement error. It is difficult to distinguish changes of the RF E-field at the level of the statistical uncertainty of the measurement, $\sim 1\%$.

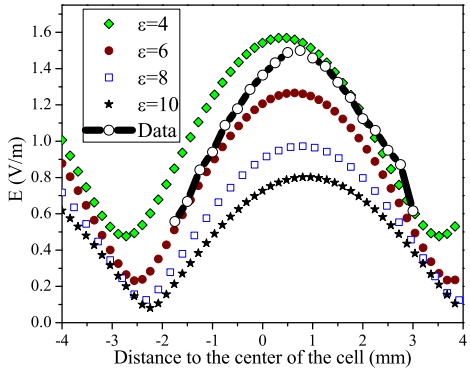

FIG. 5. (color online) 1D model results for the E-field variability between two 1 mm thick pyrex walls separated by 8 mm for different dielectric constants at 23.93 GHz. The incident E-field is $1\,\mathrm{V\,m^{-1}}$.

To further support our experimental results, we used two different theoretical models. When a RF E-field is incident onto a glass vapor cell there are two effects to understand. One is the RF FP effect and the other is polarization of the vapor cell which can also scatter RF energy, particularly at the corners of a vapor cell. We show that the FP effect is the most important one using both a full 3-dimensional (3D) finite element (FE) model of the vapor cell and a simple analytic 1-dimensional (1D) 5-layer material model. Since the FE method is a full 3D model, the geometry of the vapor cell used in the experiment can be modeled to determine the fields inside the vapor cell, including both the FP cavity effect and the effects of the corners.

The 1D 5-layer model is more straightforward and can be used to isolate the RF FP cavity effects. In the 5-layer model, the field variability inside the vapor cell can be approximated with five different regions: the region inside the vapor cell, the two pyrex walls and the surrounding free-space. In this model we assume that the pyrex walls are 1 mm thick. The vapor cell walls extend to infinity and the RF E-field is normally incident. The two pyrex walls are separated by a distance D effectively forming a planar FP cavity. This model has no corners and the E-field variation between the two pyrex walls can be easily determined analytically with a layered media approach [32].

Fig. 5 shows calculations of the spatial variation of the RF E-field inside the vapor cells for different vapor cell wall dielectric constants for the 1D model. The experimental data for the $32D_{5/2} \leftrightarrow 33P_{3/2}$ transition at 23.93 GHz is also shown in Fig. 5. The separation between the walls is D=8 mm. Fig. 6 shows the RF E-field variation for pyrex at different frequencies. We simulate the results for dielectric constant $\varepsilon = 3.0 - 5.0$ at different RF E-field frequencies because the dielectric constant can vary from the manufacturing process. The overall thickness of the vapor cell and its walls make it difficult to determine ε from the simulations. The results for the different ε are qualitatively the same as shown in Fig. 6. The results of the 1D model show the same type of FP resonances observed in the experimental data. The comparison of the 1D model results and the experimental data suggest that the variation of the RF E-field is primarily due to the FP effect and can be reduced by using smaller values

of D/λ_{RF}.

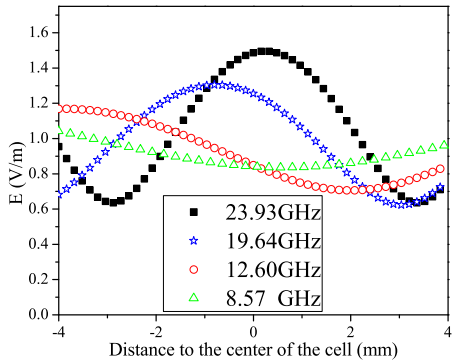

FIG. 6. (color online) 1D model results for the E-field variability between two 1 mm thick pyrex walls separated by 8 mm for different frequencies for a $1\,\mathrm{V\,m^{-1}}$ incident E-field.

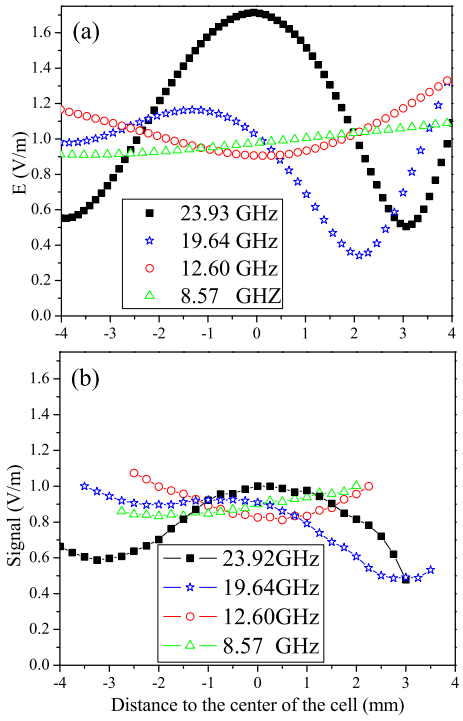

FIG. 7. (color online) RF E-field pattern in the cubic vapor cell with 8 mm inner diameter and 1 mm wall thickness. (a) The results of the 3D FE model for a $1\,\mathrm{V\,m^{-1}}$ incident E-field. (b) The experimental results.

The 3D FE model takes into account both the FP effect and the polarization of the vapor cell due to the scattering. The more detailed model allows for better comparison to the experimental data. Fig. 7 shows a comparison between the FE model calculations and the experimental data for the RF E-field inside the vapor cell at different frequencies. The 3D FE results are similar to those obtained with the 1D 5-layer analytic model as shown in Fig. 6, again, indicating that the dominate effect causing the E-field variation is due to the FP cavity effect as opposed to scattering from the corners. Fig.7 also shows qualitative agreement with the experimental results.

The main difference between the experiment and the 3D calculation is a result of surface variations of the vapor cells. During manufacture of the vapor cells, the surface can be distorted when the vapor cell is fused at high temperature. The imperfections that are created can be eliminated by using a better fabrication process, like anodic bonding to seal the vapor cell [33, 34].

Upon comparing the results from the 1D model, the FE model, and the experimental data, it is shown that the E-field variation inside the vapor cell is dominated by the FP cavity resonances. The variation can affect the accuracy of an atom-based E-field measurement. However, the results show that this E-field variation can be reduced dramatically by making the vapor cell dimension small compared to λ_{RF}, $D/\lambda_{RF} \ll 1$. When the vapor cell is designed to eliminate FP resonances, the E-field variation is less than the statistical accuracy of current measurements. It is also possible to reduce the size of the vapor cell to further reduce the effects of the vapor cell on the RF E-field measurement.

IV. CONCLUSION

Our results show that the D/λ_{RF} ratio and the dielectric constant of the vapor cell affects the accuracy of Rydberg atom-based RF E-field measurements. In fact, the variation inside the vapor cell and absorption by the vapor cell walls can ultimately affect the over-all uncertainty of a vapor cell Rydberg atom-based E-field measurement. The variation of the E-field is smaller than $\pm 0.7\%$ when the D/λ_{RF} ratio is less than 0.08. This value leads to ± 0.03 dB uncertainties in the magnitude of RF E-field. By selecting a proper D/λ_{RF} value and vapor cell material, the uncertainty due to the vapor cell can be controlled and reduced to less than current RF E-field measurement uncertainties. Vapor cells with low relative dielectric constant, as close to 1 as possible are best as long as they can maintain vacuum [25]. It is also important to consider how the signal scales with size as considered in [25]. The accuracy of Rydberg atom-based RF E-field measurements are currently not limited, in principle, by the vapor cell or its geometry. This work also shows that RF E-fields are promising for quantum manipulation of Rydberg atoms contained in small vapor cells [26, 27]. Considering the high sensitivity, large frequency range, high spatial resolution, and high accuracy of Rydberg atom-based E-field sensing, the technique is promising to become the next generation of standard for RF E-fields.

V. ACKNOWLEDGEMENT

This work was supported by the DARPA Quasar program by a grant through the ARO (60181-PH-DRP). The authors thank Harald Kübler for useful discussions.

[1] M. Koschorreck, M. Napolitano, B. Dubost, and M.W. Mitchell, "Sub-projection-noise sensitivity in broadband atomic magnetometry," Phys. Rev. Lett., **104**, 093602 (2010).

[2] W. Wasilewski, K. Jensen, H. Krauter, J.J. Renema, M.V. Balabas, and E.S. Polzik, "Quantum noise limited and entanglement-assisted magnetometry," Phys. Rev. Lett., **104**, 133601 (2010).

[3] M.V. Balabas, T. Karaulanov, M.P. Ledbetter, and D. Budker, "Polarized alkali-metal vapor with minute-long transverse spin-relaxation time," Phys. Rev. Lett., **105**, 070801 (2010).

[4] I.M. Savukov, S.J. Seltzer, M.V. Romalis, and K.L. Sauer, "Tunable atomic magnetometer for detection of radio-frequency magnetic fields," Phys. Rev. Lett., **95**, 063004 (2005).

[5] D.S. Weiss, B.C. Young, and S. Chu, "Precision measurement of the photon recoil of an atom using atomic interferometry," Phys. Rev. Lett., **70**, 2706 (1993).

[6] D.M. Pozar, *Microwave and RF design of wireless systems* (Wiley New Jersey, 2001).

[7] S.M. Davis, D.A. Landgrebe, T.L. Phillips, P.H. Swain, R.M. Hoffer, J.C. Lindenlaub, and L.F. Silva, "Remote sensing: the quantitative approach," in *Remote sensing: the quantitative approach*, Vol. 1, edited by P.H. Swain and S.M. Davis (McGraw-Hill International Book Co., New York, 1978) p. 405.

[8] E.T. Thostenson and T.-W. Chou, "Microwave processing: fundamentals and applications," Composites Part A: Applied Science and Manufacturing, **30**, 1055–1071 (1999).

[9] V.A. Tishchenko, V.I. Tokatly, and V.I. Luk'yanov, "The beginning of the metrology of radio-frequency electromagnetic fields and the first standards of electric field strength," Measurement Techniques, **46**, 76–84 (2003).

[10] J.A. Sedlacek, A. Schwettmann, H. Kübler, R. Löw, T. Pfau, and J.P. Shaffer, "Microwave electrometry with rydberg atoms in a vapour cell using bright atomic resonances," Nat. Phys., **8**, 819–824 (2012).

[11] J.A. Sedlacek, A. Schwettmann, H. Kübler, and J.P. Shaffer, "Atom-based vector microwave electrometry using rubidium rydberg atoms in a vapor cell," Phys. Rev. Lett., **111**, 063001 (2013).

[12] H.Q. Fan, S. Kumar, R. Daschner, H. Kübler, and J.P. Shaffer, "Subwavelength microwave electric-field imaging using rydberg atoms inside atomic vapor cells," Opt. Lett., **39**, 3030–3033 (2014).

[13] C.L. Holloway, J.A. Gordon, S. Jefferts, A. Schwarzkopf, D. Anderson, S. Miller, N. Thaicharoen, and G. Raithel, "Broadband rydberg atom-based electric-field probe for si-traceable, self-calibrated measurements," IEEE Transactions on Antennas and Propagation, **62**, 6169 (2014).

[14] J.A. Gordon, C.L. Holloway, A. Schwarzkopf, D.A. Anderson, S. Miller, N. Thaicharoen, and G. Raithel, "Millimeter wave detection via autler-townes splitting in rubidium rydberg atoms)," Appl. Phys. Lett., **105**, 024104 (2014).

[15] C.L. Holloway, J.A. Gordon, A. Schwarzkopf, D.A. Anderson, S.A. Miller, N. Thaicharoen, and G. Raithel, "Sub-wavelength imaging and field mapping via electromagnetically induced transparency and autler-townes splitting in rydberg atoms," Appl. Phys. Lett., **104**, 244102 (2014).

[16] A.K. Mohapatra, T.R. Jackson, and C.S. Adams, "Coherent optical detection of highly excited rydberg states using electromagnetically induced transparency," Phys. Rev. Lett., **98**, 113003 (2007).

[17] A.K. Mohapatra, M.G. Bason, B. Butscher, K.J. Weatherhill, and C.S. Adams, "A giant electro-optic effect using polarizable dark states," Nat. Phys., **4**, 890 (2008).

[18] M.G. Bason, M. Tanasittikosol, A. Sargsyan, A.K. Mohapatra, D. Sarkisyan, R.M. Potvliege, and C.S. Adams, "Enhanced electric field sensitivity of rf-dressed rydberg dark states," New J. Phys., **12**, 065015 (2010).

[19] M. Fleischhauer, A. Imamoglu, and J.P. Marangos, "Electromagnetically induced transparency: Optics in coherent media," Rev. Mod. Phys., **77**, 633 (2005).

[20] D.C. Paulusse, N.L. Rowell, and A. Michaud, "Accuracy of an atomic microwave power standard," Instrumentation and Measurement, IEEE Transactions on, **54**, 692–695 (2005).

[21] T.P. Crowley, E.A. Donley, and T.P. Heavner, "Quantum-based microwave power measurements: Proof-of-concept experiment," Rev. Sci. Instrum., **75**, 2575–2580 (2004).

[22] F. Dolde, H. Fedder, M.W. Doherty, T. Nöbauer, F. Rempp, G. Balasubramanian, T. Wolf, F. Reinhard, L.C.L. Hollenberg, F. Jelezko, and J. Wrachtrup, "Electric-field sensing using single diamond spins," Nat. Phys., **7**, 459–463 (2011).

[23] V.M. Acosta, K. Jensen, C. Santori, D. Budker, and R.G. Beausoleil, "Electromagnetically induced transparency in a diamond spin ensemble enables all-optical electromagnetic field sensing," Phys. Rev. Lett., **110**, 213605 (2013).

[24] D.A. Steck, *Cesium D line data revision 2.1.4* (2010).

[25] H.Q. Fan, S. Kumar, J. Sedlacek, Kübler, S. Karimkashi, and J. P. Shaffer, "Atom based rf electric field sensing," J. Phys. B: At., Mol. Opt. Phys., **48**, 202001 (2015).

[26] H. Kübler, J.P. Shaffer, T. Baluktsian, R. Löw, and T. Pfau, "Coherent excitation of rydberg atoms in micrometre-sized atomic vapour cells," Nat. Photon., **4**, 112–116 (2010).

[27] A. Urvoy, F. Ripka, I. Lesanovsky, D. Booth, J.P. Shaffer, T. Pfau, and R. Löw, "Strongly correlated growth of rydberg aggregates in a vapour cell," Phys. Rev. Lett., **114**, 203002 (2015).

[28] M.J. Piotrowicz, C. MacCormick, A. Kowalczyk, S. Bergamini, I.I. Beterov, and E.A. Yakshina, "Measurement of the electric dipole moments for transitions to rubidium rydberg states via autler–townes splitting," New J. Phys., **13**, 093012 (2011).

[29] M. Marinescu, H.R. Sadeghpour, and A. Dalgarno, "Dispersion coefficients for alkali-metal dimers," Phys. Rev. A, **49**, 982 (1994).

[30] Y. Duan, H. Ma, X. Li, S. Liu, and Z. Ji, "The microwave electromagnetic characteristics of manganese dioxide with different crystallographic structures," Physica B: Condensed Matter, **405**, 1826 – 1831 (2010), ISSN 0921-4526.

[31] W.B. Westphal, *Technical Report AFML-TR-74-250. Dielectric constant and loss data* (Laboratory for Insulation Research, Massachuesetts Institute of Technology, 1977).

[32] L. Brekhovskikh, *Waves in Layered Media* (Academic Press, London, 1960).

[33] R. Daschner, R. Ritter, H. Kübler, N. Frühauf, E. Kurz, R. Löw, and T. Pfau, "Fabrication and characterization of an electrically contacted vapor cell," Opt. Lett., **37**, 2271–2273 (2012).

[34] D. Barredo, H. Kübler, R. Daschner, R. Löw, and T. Pfau, "Electrical readout for coherent phenomena involving rydberg atoms in thermal vapor cells," Phys. Rev. Lett., **110**, 123002 (2013).